

Characterization of the large-size NDL EQR20 silicon photomultipliers

Yu. A. Melikyan^{a,1}, I.G. Bearden^b, V. Buchakchiev^c, S. Jia^b, V. Kozhuharov^c and I. P. Møller^b

^a *Helsinki Institute of Physics, University of Helsinki, P.O. Box 64, FI-00014, Finland*

^b *Niels Bohr Institute, University of Copenhagen, Jagtvej 155A, 2200 Copenhagen, Denmark*

^c *Faculty of Physics, Sofia University "St.Kliment Ohridski", 5 J. Bourchier Blvd, 1164 Sofia, Bulgaria*

Keywords: Silicon photomultipliers, SiPM, NDL, scintillator-based calorimetry

Abstract

Unlike most commercially available silicon photomultipliers (SiPMs), EQR20 SiPMs produced by the Novel Device Laboratory (NDL) avoid using individual resistors to quench the avalanche multiplication of the microcells. Instead, bulk resistance of the epitaxial silicon layer is used, and the signal is directly collected at a common anode plane. This allows for the fabrication of SiPMs as large as $6.2 \times 6.2 \text{ mm}^2$ while keeping the recovery time below $\tau = 25 \text{ ns}$. These devices can be composed of microcells with $20 \text{ }\mu\text{m}$ pitch while reaching PDE above 50% and 10^6 gain at 5 V overvoltage. On the other hand, a crosstalk level from 20% to 40% is observed for overvoltages from 3 V to 5 V. Moreover, significant pulse shape distortion is observed once the microcell occupancy exceeds a few percent. This work provides an independent determination of the performance parameters of the EQR20 11-6060D-S SiPMs and discusses the influence of the pulse shape distortion on the applicability of these devices in a scintillator-based calorimeter of a hadron collider experiment.

1. Introduction

The Silicon Photomultiplier (SiPM), also known as Multi-Pixel Photon Counter (MPPC), is a modern photosensor for low-intensity light detection [1, 2]. Composed of thousands of individual micron-scale single-photon avalanche diodes (SPADs), which we refer to as microcells below, SiPMs produce an electronic signal proportional to the number of detected photons. The signal produced by one microcell is independent of the number of photons detected in it. Therefore, the proportionality between the number of detected photons and the signal charge deviates from linear once the Poisson probability of simultaneous detection of more than one photon in the same microcell becomes significant.

To extend the linear range of SiPM operation, a single SiPM must comprise a larger number of microcells. Reducing the microcell size has its limits, since it causes a reduction of the photon detection efficiency (PDE) and gain of the device [3, 4]. Substrates of larger area (e.g. $6 \times 6 \text{ mm}^2$ or more) allow for SiPMs of larger number of microcells, thus increasing the useful dynamic range in terms of light intensity. Being directly proportional to the SiPM area, the capacitance grows significantly, extending the recovery time and the trailing edge of the output signal considerably [5], often exceeding $\tau = 100 \text{ ns}$.

A widespread SiPM production technology uses quenching resistors to connect each individual microcell with the power line [2]. In contrast, the so-called “EQR” technology relies on the bulk resistance of the epitaxial silicon layer to quench the avalanche multiplication process and recover the microcell [3, 5]. Avalanche electrons are directly collected at a common anode on the device’s surface. Minimizing the blind area at the SiPM input and reducing the terminal capacitance, this

¹ Corresponding author

technology allows the production of large-size SiPMs featuring much higher PDE and much faster recovery than the current widespread production technology [6].

Figure 1 clearly illustrates the difference in response of a pair of otherwise similar SiPMs produced according to the two different technologies.

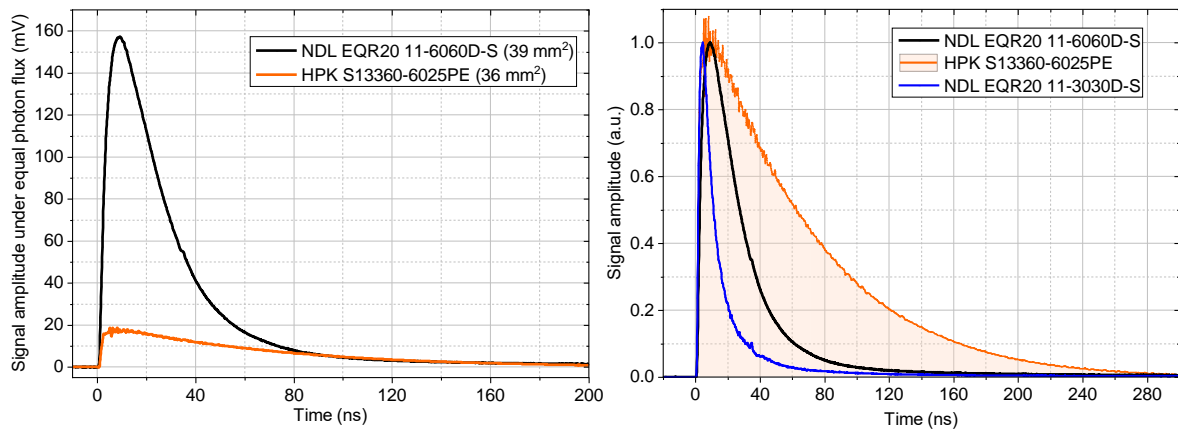


Figure 1. Left - response of an NDL EQR20 SiPM (39 mm^2) and a Hamamatsu S13360-6025 SiPM with individual quenching resistors (36 mm^2) to a sub-ns flash of 440 nm light. The pulse shapes were averaged over 2000 waveforms measured at 5 V overvoltage under an equal photon flux of 25 photons / mm^2 / pulse. The mismatch in the pulses' height and width are due to the different PDE, gain, crosstalk, sensitive area and RC of the devices. Right – same data reproduced with each pulse normalized to its peak amplitude. The blue signal is from a smaller NDL EQR20 SiPM, sized $3 \times 3 \text{ mm}^2$, measured under the same photon flux at 4.7 V overvoltage.

The advantages of the EQR technology for the photon readout in a scintillator-based calorimeter of an accelerator experiment, such as the ALICE FoCal-H project [7], are:

- A combination of the high PDE and high dynamic range can provide freedom to choose the number of scintillation fibers read out by a single SiPM, thus optimizing the detector granularity and cost.
- A shorter pulse width and faster recovery can extend the operability of a SiPM when its dark count rate is increased as a result of radiation damage.
- Faster recovery also extends the rate capability of the device, particularly relevant given the 25 ns spacing between the two adjacent bunches of HL-LHC [8].

EQR SiPMs with 20 μm microcell size and sensitive area of up to 39 mm^2 are commercially available from Novel Device Laboratory (NDL) [6]. The scarce data on their performance available in literature did not allow us to determine if the EQR SiPMs indeed outperform those produced according to the widespread technology in the application specified above. Therefore, we have performed a dedicated characterization of the NDL EQR20 11-6060D-S SiPMs, and the results are provided here.

2. The experimental set up and measurement program

The schematic of the experimental setup is provided in Fig. 2. Two or more SiPMs were tested simultaneously in a light-tight box. For the dark noise measurements, an external light absorber was added around the SiPM input window, thus ensuring no photons scattered from inside one photosensor under study get detected in the others. Those measurements related to external photon detection were done with pulsed light produced by a picosecond laser monitored by a reference photosensor (Panacon XP85002/FIT-Q PMT [9]). We used a Picoquant PDL800-B laser with an LDH-P-C-440M laser head. It features $440 \text{ nm} \pm 10 \text{ nm}$ wavelength, $\leq 20 \text{ ps}$ jitter and $\leq 55 \text{ ps}$ pulse width [10].

The laser beam was defocused by an optical fiber coupler and passed through an optical attenuator. With $\pm 13^\circ$ aperture of the multimode fiber used, output light was projected to a diffuse white reflector, ensuring a spot large enough to provide a homogeneous photon flux distribution across the sensitive area of all photosensors used in the set up. The spread in the photon flux across all photosensors was $< 1\%$ - see [9] for the detailed description and results of the homogeneity measurement. This allowed us not only to test different SiPMs under the same photon flux but also to measure its absolute value thanks to the known sensitive area, quantum efficiency, collection efficiency and gain of the reference PMT [9].

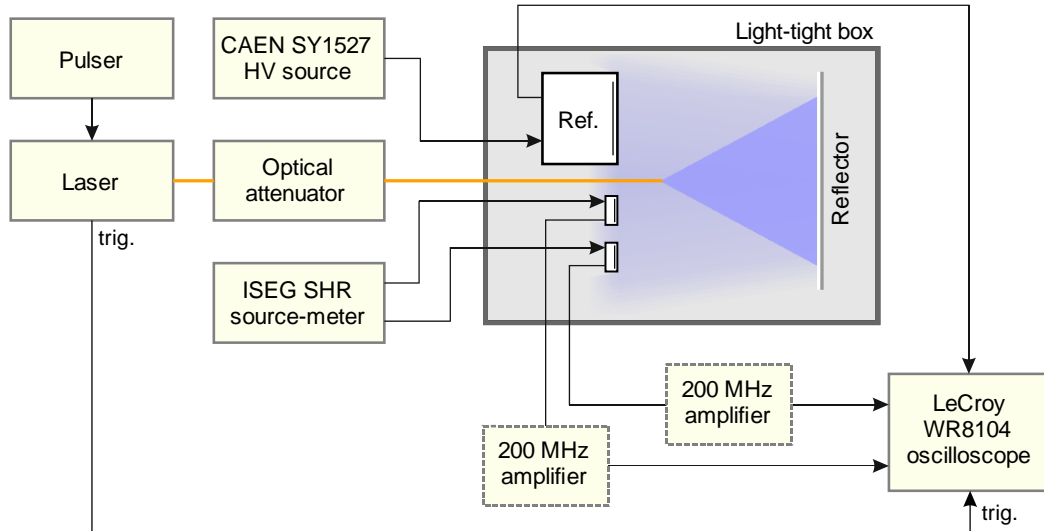


Figure 2. Schematic of the experimental set up. The 200 MHz amplifiers were used in a subset of measurements.

Positive bias voltage was supplied to SiPM cathode using the basic connection circuit recommended by the manufacturer – see Fig. 3.

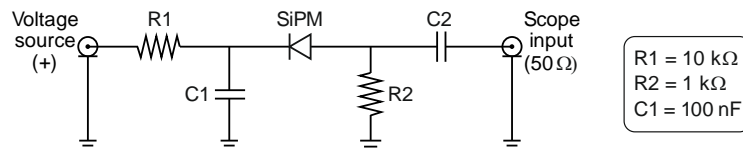


Figure 3. The simplest SiPM connection diagram recommended by the manufacturer was used [6]. R1, R2, and C1 values were kept constant in all cases, while the coupling capacitance C2 was shorted or altered in different measurements, as reflected in the text.

The measurement program was intended to verify and complement those NDL specification parameters relevant to the possible SiPM application for scintillation photon readout of the future ALICE FoCal hadron calorimeter [7]:

- breakdown voltage defined from bias I-V curves and from relative gain measurement;
- pulse shape stability at various overvoltages;
- effect of the optical crosstalk between microcells derived from the dark noise spectra;
- visible value of the dark count rate (DCR) and the true DCR value derived based on the actual pulse shape;
- absolute PDE corrected for the crosstalk value;
- response linearity and pulse shape stability versus absolute flux of the incoming photons;
- response as a function of the time between two consecutive pulses and their intensity.

3. Results

3.1. Breakdown voltage

SiPM breakdown voltage at 26 ± 1 °C was determined using two independent experimental techniques. First, the bias voltage of tested SiPMs was increased at a 0.05 V/s rate, which is slow enough to spot the rise in bias current characteristic for the region of avalanche multiplication with $V_{\text{bias}} > V_{\text{br}}$. The I-V curves measured for two tested SiPMs of the same type are shown in Fig. 4.

The standard deviation of the leakage current is $\sigma(I_{\text{leakage}}) \approx 3$ nA. We determined V_{br} as the visible starting point of the rise of dark current once I_{dark} exceeds $2 * \sigma(I_{\text{leakage}})$. The result is $V_{\text{br}} = 27.4$ V for both tested SiPMs, in agreement with the typical $V_{\text{br}} = 27.5$ V outlined in the datasheet [6].

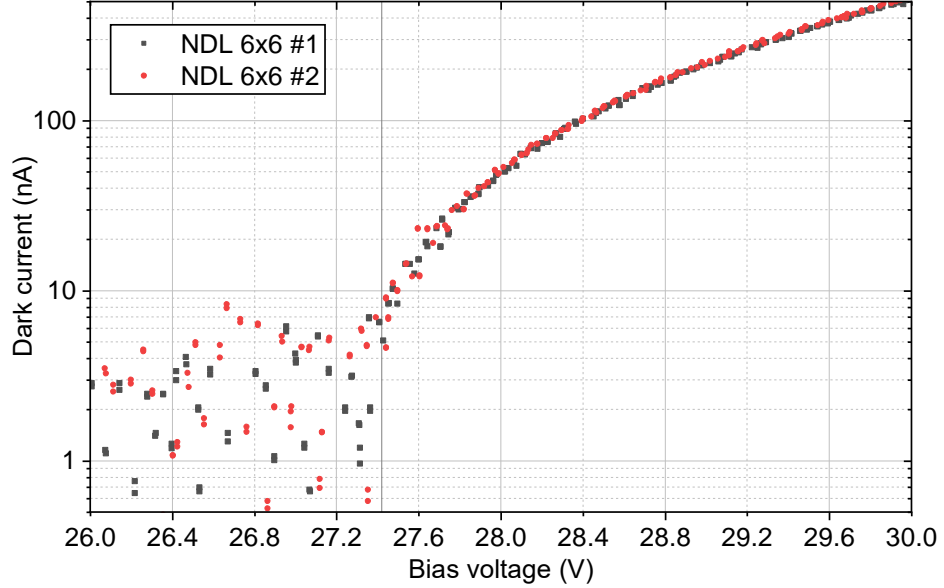


Figure 4. Dark current dependence on the bias voltage for two NDLEQR20 11-6060D-S SiPMs as measured by the ISEG SHR 4260 source-meter at 0.05 V/s ramp speed.

The V_{br} determination result was cross-checked independently for NDLEQR20 SiPM #1 by measuring the charge spectra of the dark signals passed via an external 200 MHz LeCroy 612M amplifier. Typical spectra measured above the detection threshold of 0.5 photoelectrons (p.e.) at various overvoltages are shown in Fig. 5.

A combined fit of multi-gaussian peaks with a common baseline function was used to define the positions of individual peaks [11]. The single photoelectron (SPE) charge was defined as the difference in the fitted means of 2 p.e. and 1 p.e. peaks. The linear nature of the SPE charge dependence on the overvoltage was used to define the breakdown voltage, as shown in Figure 6. The result, $V_{\text{br}} = 27.42 \text{ V} \pm 0.04 \text{ V}$, agrees perfectly with the result of the V_{br} determination from the IV curve described above.

3.2. Absolute gain

The dependence of the absolute gain on the SiPM overvoltage can be derived from the data shown in Fig. 6 by correcting the vertical scale for the gain of the external amplifier. However, to avoid the possible influence of the amplifier's integral and differential nonlinearities on the calculation result, we measured the SPE charge spectra of low-intensity laser pulses at $V_{\text{ov}} \approx 5$ V directly, bypassing the amplifier. With pulses as narrow as 1.5 mV/pC (see Fig. 1), the large-size NDLEQR20 SiPM feature sufficient SPE resolution to distinguish the discrete structure of the pedestal, 1 p.e. and 2 p.e. peaks.

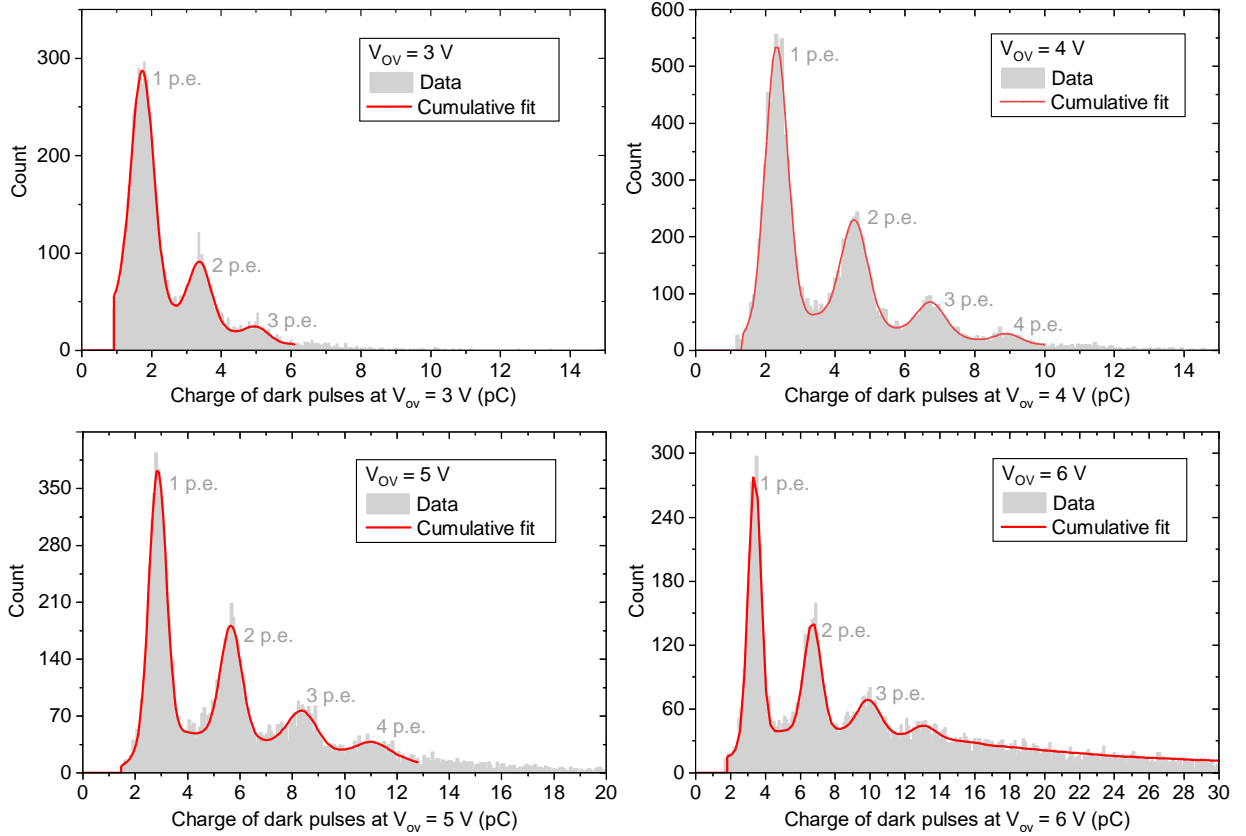


Figure 5. Charge spectra of dark pulses of an NDL SiPM sized $6.24 \times 6.24 \text{ mm}^2$ measured at overvoltages from 3 V to 6 V. An external amplifier was used to better distinguish the discrete peaks at low overvoltage.

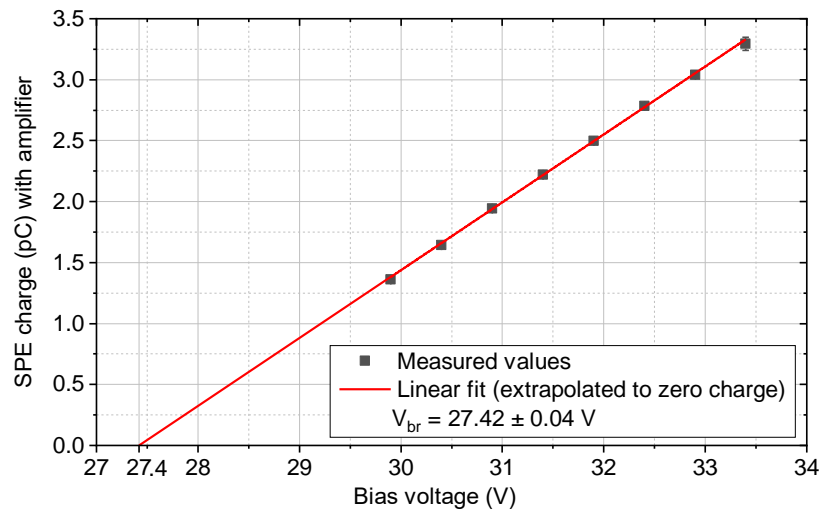


Figure 6. Determination of the breakdown voltage of the NDL SiPM sized $6.24 \times 6.24 \text{ mm}^2$ from the SPE charge dependence on the bias voltage.

The absolute SPE charge measured at three different bias voltages is shown in Fig. 7, along with the V_{br} value defined in sec. 3.1. The linear fit of the four available points shows the dependence of the absolute gain (G) on the overvoltage. As can be seen from the fit, the NDL EQR20 SiPM features absolute gain as high as $5.7 \cdot 10^5$ at $V_{ov} = 3 \text{ V}$, almost reaching the gain of 10^6 at $V_{ov} = 5 \text{ V}$. Given the relatively small microcell pitch of $20 \mu\text{m}$, this value is competitive with SiPMs having individual quenching resistors [4, 12].

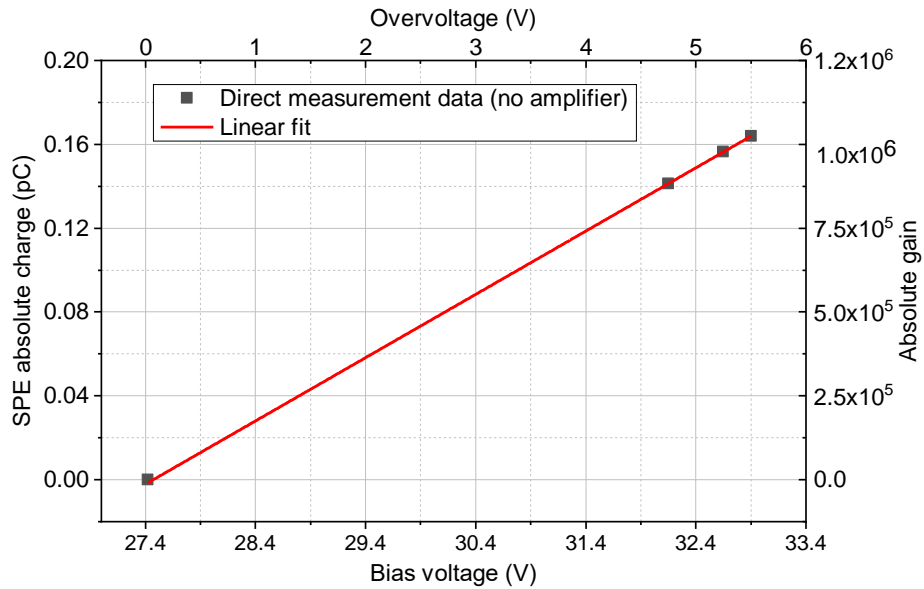


Figure 7. The mean value of the SPE charge measured without the external amplifier. Error bars are smaller than the data point symbols. Having the V_{br} value known, the linear fit of the combined data represents the dependence of absolute gain (indicated on the right vertical axis) of NDL EQR20 SiPM versus overvoltage.

3.3. Pulse shape stability versus overvoltage

NDL EQR20 SiPMs show some variation of the pulse shape at different overvoltages measured with the same incident light intensity. Pulses from low-intensity laser illumination ($\sim 0.2\%$ microcells occupancy at $V_{ov} = 3$ V) become shorter while increasing V_{ov} from 2.5 V up to 5 V. At even larger overvoltage, the pulses become longer – see Fig. 8. Detailed quantitative parameters of the rise time (t_{rise} , the time difference between signal crossings at relative amplitude thresholds) and the fall time (τ_{fall} , the characteristic time of the trailing edge fitted with an exponential function) are provided in Fig. 9 as a function of the overvoltage. When using the DC-coupled SiPM circuit (C2 shorted), the $t_{rise} = 5.3$ ns at $V_{ov} = 2.5$ V, dropping to $t_{rise} = 4.4$ ns just below $V_{ov} = 5$ V; above that, the rise time grows again, reaching $t_{rise} = 5.6$ ns at $V_{ov} = 6$ V. Fall time changes from $\tau_{fall} = 28$ ns at 2.5 V overvoltage, dropping to 22 ns before increasing to 34 ns at $V_{ov} = 6$ V.

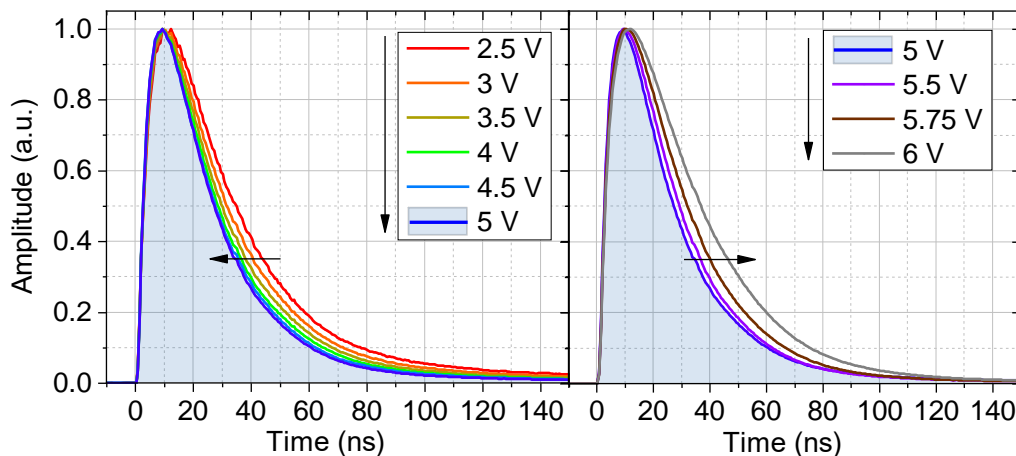


Figure 8. Pulse shapes of the same NDL EQR20 SiPM under picosecond laser illumination at different overvoltages. For overvoltages from 2.5 to 5 V, the pulse narrows and then broadens for overvoltages above 5 V.

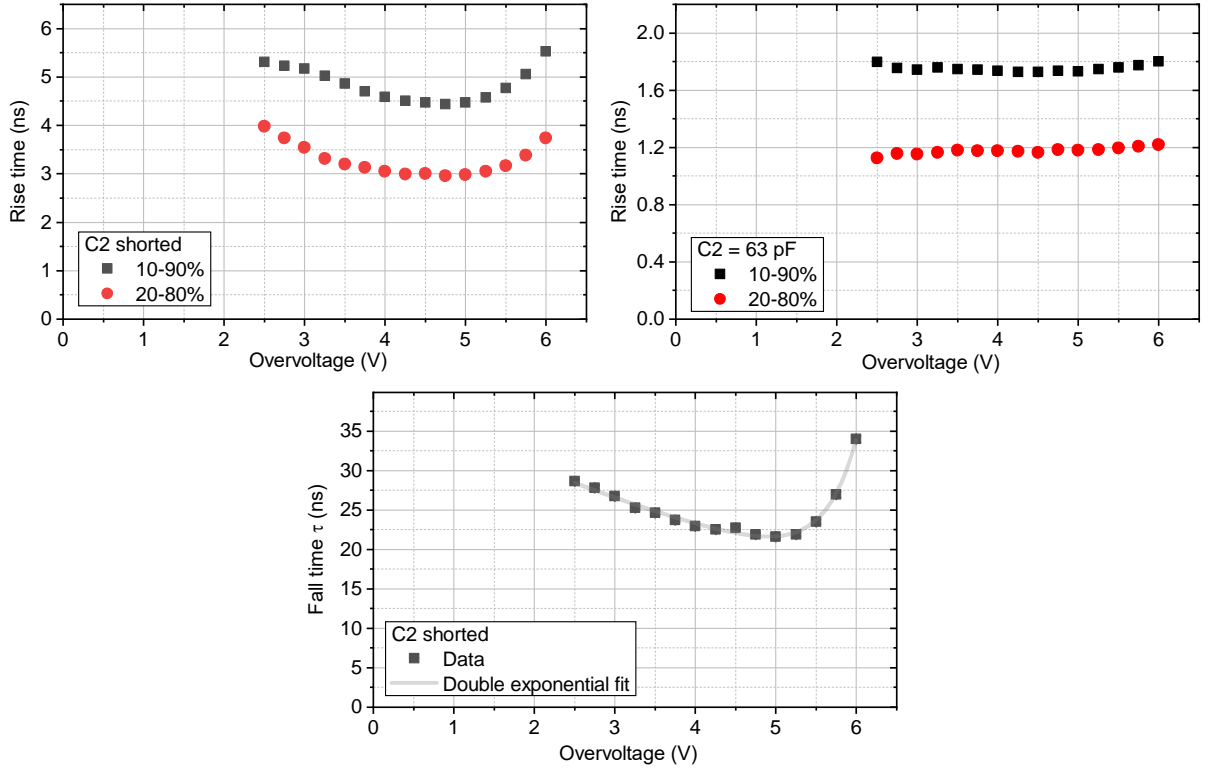


Figure 9. Top: interpolated rise time of an NDL EQR20 SiPM sized $6.24 \times 6.24 \text{ mm}^2$ under low-intensity picosecond laser illumination. The left graph is for the case when no coupling capacitance is used (C_2 , see Fig. 3). The right graph was measured with $C_2 = 63 \text{ pF}$. Bottom: characteristic time of the trailing edge fitted with an exponent function (τ_{fall}). The resulting dependence of τ_{fall} versus V_{ov} can be fit with a double exponential (adj. R-square = 0.982).

3.4. Dark count rate and optical crosstalk

Operating at room temperature, large-area SiPMs suffer from high dark count rates (DCR) on the order of MHz. Given also the significant pulse width ($\text{FWHM} > 30 \text{ ns}$), the probability of two uncorrelated dark pulses randomly overlapping in time becomes significant. This affects the visible value of DCR determined using a simple threshold (e.g., 0.5 p.e.). It also affects the visible value of prompt crosstalk (CT) level defined according to the standard technique (number of dark pulses with amplitude above 1.5 p.e. divided by the number of dark pulses with amplitude above 0.5 p.e. [13]). To obtain the true value of DCR and the true value of CT, we measure their “visible” values and use a simplified Monte-Carlo simulation to extract the true values from the visible ones.

In our technique of measuring the visible DCR, the first dark pulse is detected once its amplitude exceeds 0.5 p.e. in a single rise. The counter is then deactivated until the waveform crosses the 0.5 p.e. threshold again in the opposite direction. Regardless of the total pulse amplitude (i.e. even in case of a statistical pile-up), only one dark pulse is counted until the waveform falls below 0.5 p.e. Afterwards, another dark pulse is counted only if the waveform both exceeds the 0.5 p.e. threshold again and has a rise of at least 0.5 p.e. in a single event.

The simulated curve used to reconstruct the true DCR value from the measured (“visible”) one is shown in blue in Fig. 10. The dashed red line shows another derivative of the same simulation – the ratio of the purely statistical overlap of two or more pulses (resulting in signal amplitudes above 1.5 p.e.) to the visible DCR. By definition, the latter parameter does not include any correlated noise, but only a random overlap in time of multiple dark pulses. Therefore, subtracting the simulated statistical contribution from the visible CT value results in the true CT.

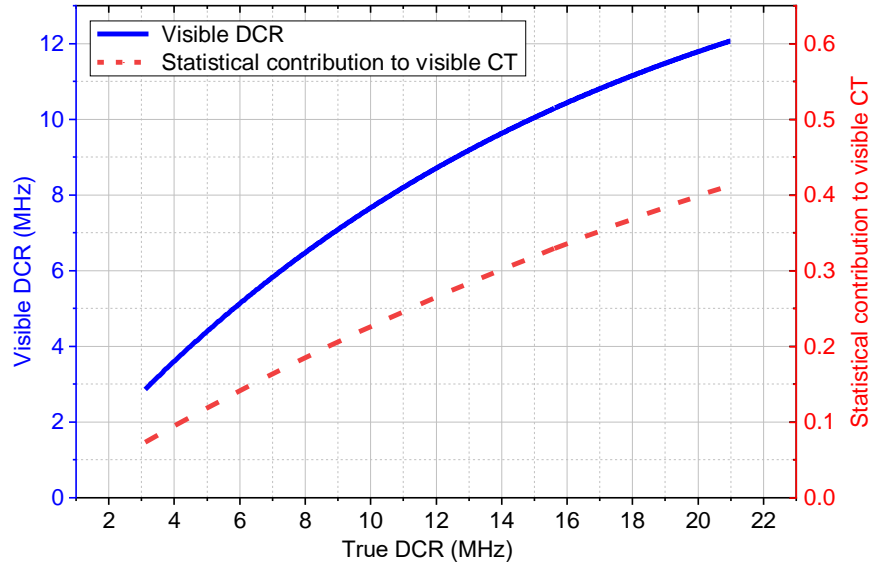


Figure 10. Statistical corrections to the visible DCR and visible CT values simulated for the pulse shapes of the NDL EQR20 SiPM sized 6.24 x 6.24 mm².

Figure 11 represents in black the “raw” results on the DCR and CT as measured according to the simplistic techniques: fixed 0.5 p.e. threshold for the DCR and a “blind” ratio of the number of dark counts with 1.5+ p.e. and 0.5+ p.e. amplitude. The points of Fig. 11 marked with red circles are based on the same experimental data but corrected for the simulated dependencies from Fig. 10, thus representing the true DCR and prompt crosstalk.

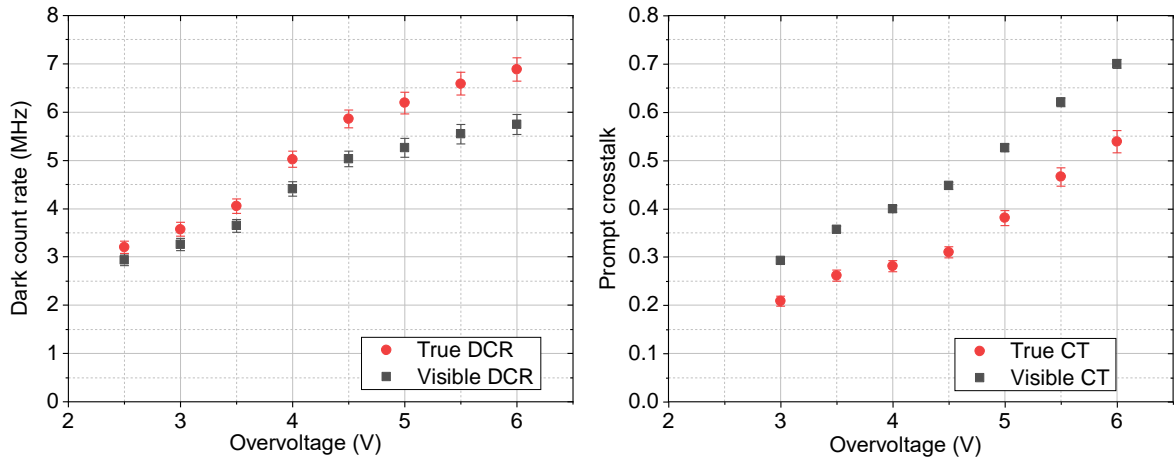


Figure 11. Dark count rate and prompt crosstalk measured at 25°C as a function of the overvoltage of the NDL EQR20 SiPM sized 6.24x6.24 mm².

3.5. Photon detection efficiency

Absolute photon detection efficiency (PDE) was measured under pulsed light ($\lambda = 440$ nm) as a ratio between the signal charge detected by the NDL SiPM and the photon flux detected by the reference PMT. The charge of the NDL signal was counted in p.e. using the absolute gain from Fig.7 and corrected for the crosstalk shown in Fig.11. Photon flux was uniformly distributed across the area of the reference PMT and tested SiPM (variation of the light distribution $<1\%$, see Sec.2 in [9]). It allowed to derive the number of photons per pulse per area hitting the SiPM thanks to the precisely known parameters of the Planacon PMT. The result is shown in Figure 12 – NDL EQR20 SiPM features remarkably high PDE for 440 nm light of 47 ± 3 (%) at $V_{ov} = 3$ V and 55 ± 4 (%) at $V_{ov} = 5$ V.

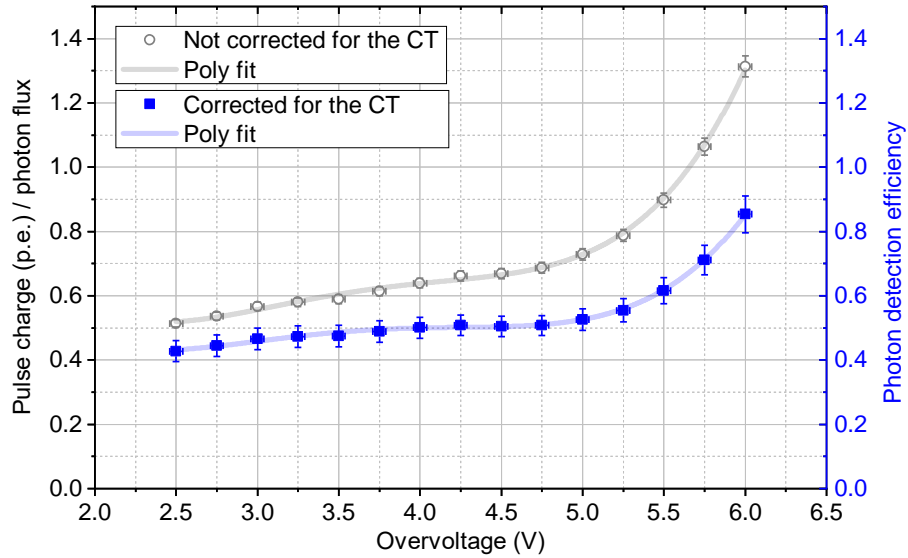


Figure 12. Photon detection efficiency of the NDL EQR20 SiPM sized 6.24 x 6.24 mm². The gray circles show the uncorrected data, while the blue squares show the data corrected for cross talk as explained in the text.

3.6. Dynamic range and linearity

The saturation curve was measured for the NDL EQR20 SiPM, and it was cross-checked with a Hamamatsu S13360 SiPM placed in the same laser light spot. Both SiPMs had similar sensitive area, but different pitch and number of microcells (NDL: 20 μm pitch, 39 mm² area, 97344 microcells; Hamamatsu: 25 μm pitch, 36 mm² area, 57600 microcells). The results are shown in Fig.13.

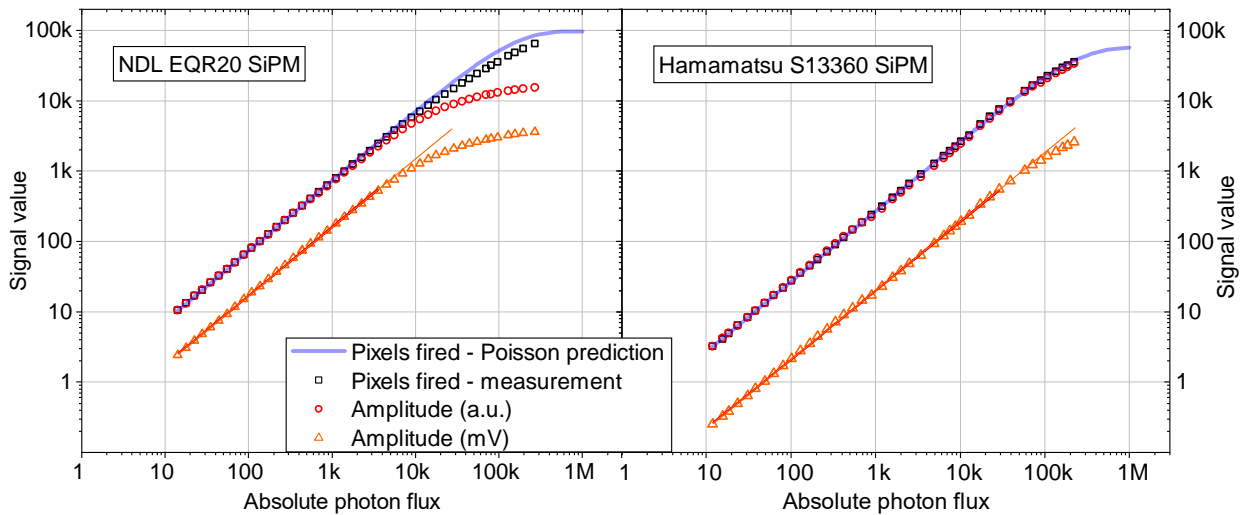


Figure 13. Output signal intensity integrated over a 600 ns-wide time window versus input light intensity for the NDL EQR20 SiPM with 97k microcells and Hamamatsu S13360 SiPM with 57k microcells. Coupling capacitance C2 was shorted for both devices.

Note the “Poisson prediction” curve is calculated independently of the output pulse measurement. It is a pure Poisson expectation from the photon flux measured in absolute units corrected for the PDE and CT values from the independent measurements reported above for the NDL EQR20 SiPM. Therefore, Fig.13 provides also a cross-check of those values. The same curve for the Hamamatsu S13360 SiPM is calculated from the specification data available from the manufacturer [4].

The Hamamatsu SiPM saturation curves both in terms of signal amplitude and charge behave in line with the Poisson prediction – experimental data deviates by less than 5% throughout the entire intensity range (up to 60% microcell occupancy reached in this measurement). The NDL curves deviate by more than 5% at microcell occupancies above 1% and 3% for amplitude and charge dependencies respectively. At 60% microcell occupancy, the amplitude deviates down to 23% of the predicted value, charge - to 72%.

The significant deviations of the NDL EQR20 response curves above 1% microcell occupancy are a sign of their pulse shape distortion. Fig. 14 provides the actual waveforms captured at various photon fluxes. The quantitative details are summarized in Fig. 15. As can be seen from Fig. 14 and 15, larger occupancies shorten the rise time and extend the trailing edge of the NDL EQR20 SiPMs, while the signals of Hamamatsu S13360 remain stable. Fall time τ_{fall} of the NDL pulse exceeds 100 ns at larger occupancies, thus reducing the signal charge from the expected value as long as it is integrated over a limited time window (600 ns in our case). A similar effect characteristic for the NDL EQR SiPMs of other types was reported [5]. The mismatch between the experimental and simulated dynamic range of the 6 μm -pitch NDL SiPM reported in [14] is likely a consequence of the same effect.

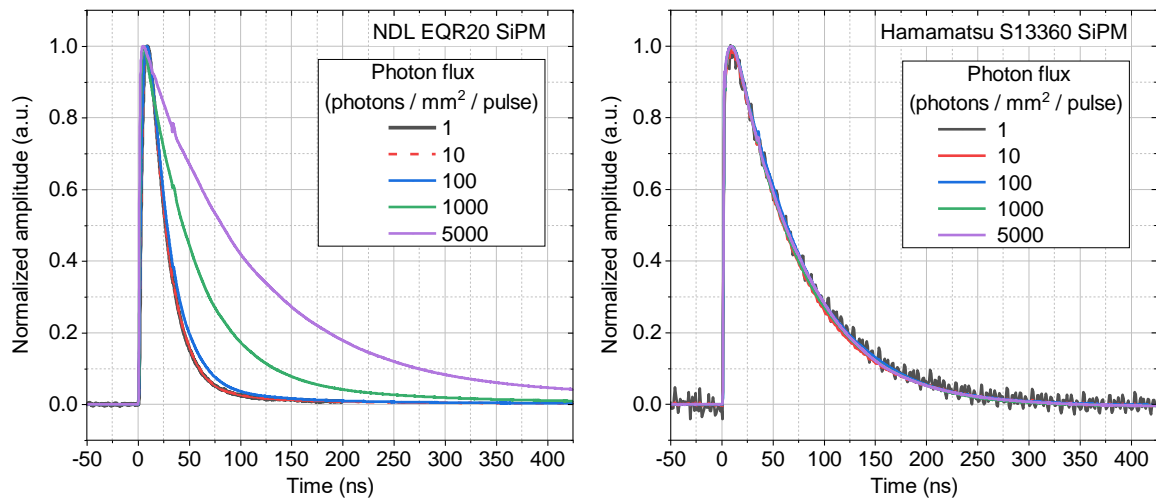


Figure 14. Waveforms of SiPM signals under picosecond laser illumination of various intensity.

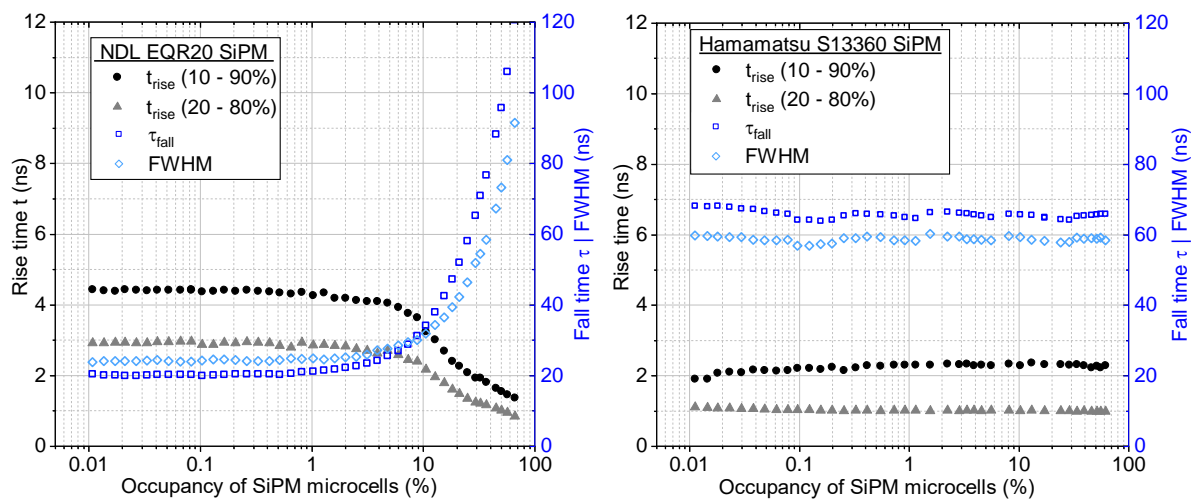


Figure 15. Rise time (t_{rise}), fall time (τ_{fall}) and interpolated FWHM of signals of the NDL and Hamamatsu SiPMs as a function of the microcell occupancy.

3.7. Rate capability

The rate capability of the NDL EQR20 SiPM was studied from the perspective of their possible application to a future hadron calorimeter for the ALICE upgrade at HL-LHC. We estimated variation in the SiPM response under bursts of two pulses coming at a low rate (100 Hz) but with very short spacing (down to 25 ns). This technique can help to estimate the limits of scintillation fiber grouping to the same SiPM and also make a comparative study between two different SiPMs. We, therefore, simultaneously measured the performance of the NDL EQR20 11-6060D-S and Hamamatsu S13360-6025PE SiPMs. Variation of the SiPM response for the second pulse in a burst dependent on spacing between the two pulses in a burst was measured at four different light intensities (from 10 photons / mm² / pulse to 3800 photons / mm² / pulse). The results are shown in Fig.16 as four plots, each with a pair of curves measured at the same pulse intensity.

A fair comparison of the performance of the NDL and Hamamatsu SiPMs based on Fig.16 is complicated due to the very different PDE and CT values of the two SiPM types. The experimental data was therefore rearranged in Fig.17 to reflect the difference in the number of microcells fired under the same pulse intensity. The shaded areas for the two SiPM types overlap, highlighting their similar performance: the NDL advantage of a larger number of microcells is counterbalanced by the drastic increase of τ_{fall} (and thus the recovery time) at larger pixel occupancies.

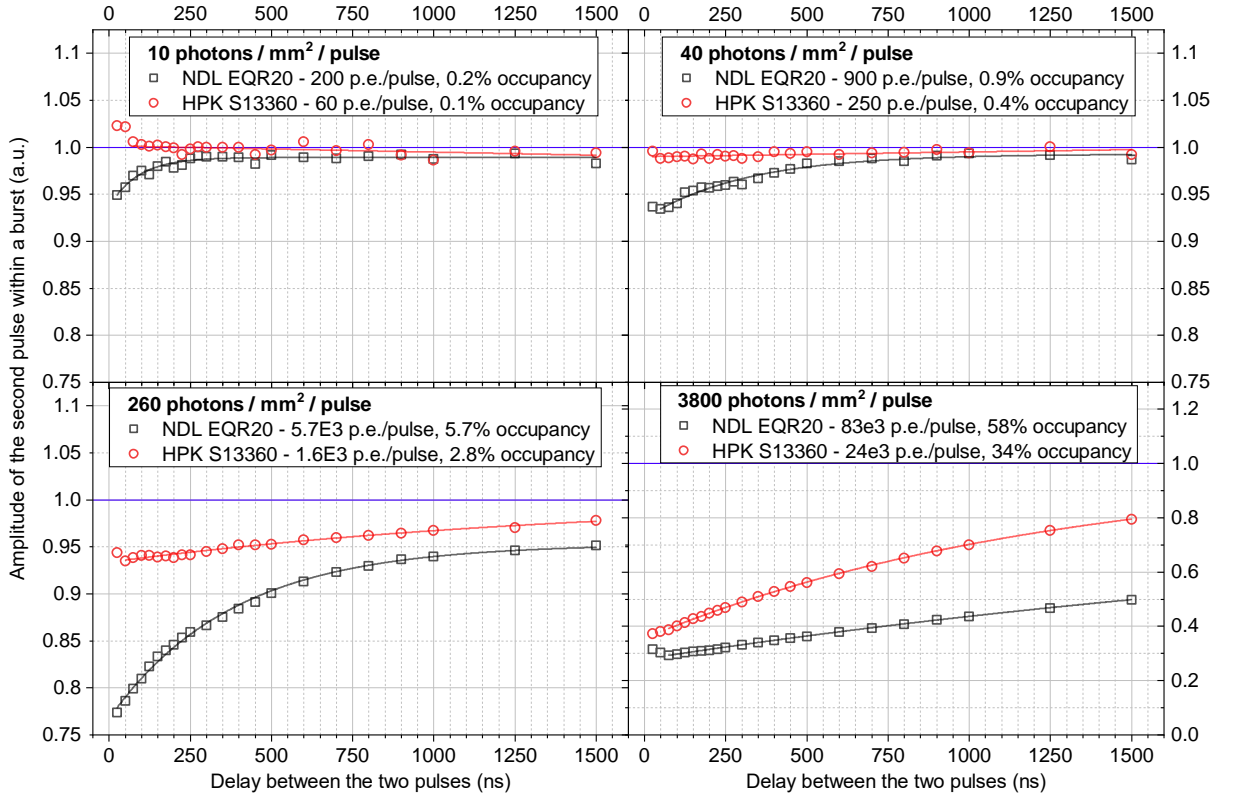


Figure 16. SiPM response as a function of the time between two consecutive pulses and their light intensity.

4. Discussion

While other key performance parameters of the NDL EQR20 SiPMs allow for their application as a photon readout option in the scintillator-based hadron calorimeter, the pulse shape distortion as a function of the microcell occupancy poses a significant complication for signal processing and detector calibration.

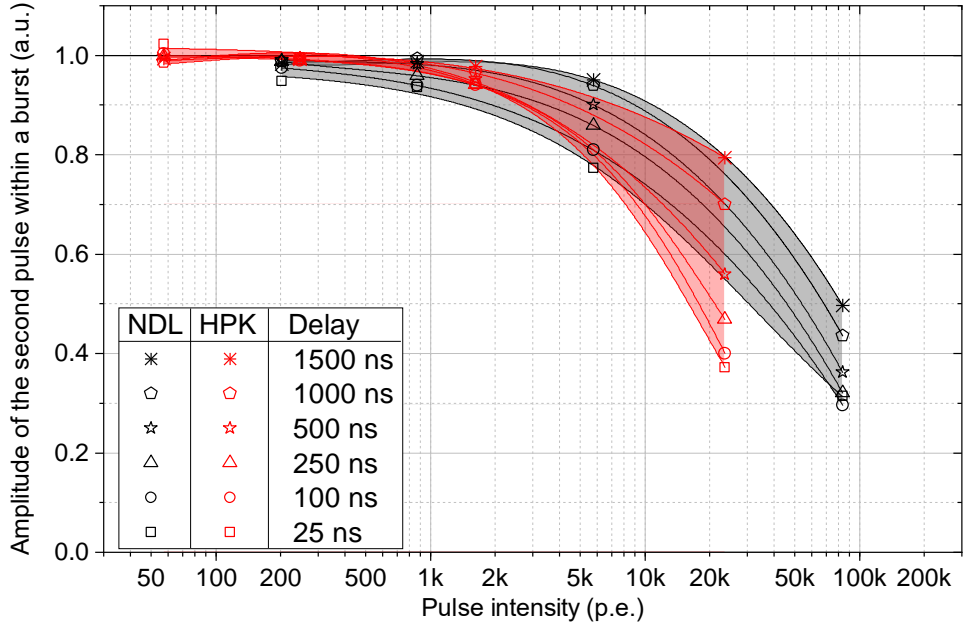


Figure 17. SiPM response as a function of the time interval between two consecutive pulses and their intensity in terms of the pulse intensity, i.e. the number of microcells fired.

The nature of the NDL SiPM pulse shape distortion is discussed in [5] from the perspective of the recovery time variation dependence on the number of pixels fired. According to [5], it is caused by a combination of capacitive effects and signal propagation delays across the device. When more microcells are fired, the simultaneous recovery and recharging of multiple cells cause pulse broadening. This broadening results from a transmission line effect, where signals from different microcells have varying delays before reaching the electrode. However, we did not see any significant difference between the saturation curves measured using a picosecond laser illumination (~ 55 ps-long) or BCF-12 scintillator pulses ignited by a pulsed UV LED (~ 10 ns-long). Also, the trends of the timing parameters shown in Fig. 15 are flat up to $\sim 1\%$ occupancy. Therefore, the statements from [5] on the nature of the pulse shape distortion are unlikely to be fully applicable for the large-size EQR20 SiPMs.

Apart from a Poisson-based correction of the signal amplitude applicable to any SiPM type, NDL EQR20 SiPMs require additional correction to reconstruct the linear dependence between the input pulse intensity and output signal amplitude. Moreover, the distortion of the signal shape affects the results of time-over-threshold (TOT) measurement. Extension of the pulse tail not only reduce the TOT dynamic range, but, depending on the threshold used, can create ambiguity in signal charge reconstruction from TOT readings if a coupling capacitance is used. See Fig.18 for the comparison of pulse shapes in log scale measured with the coupling capacitance C2 shorted (top-left) and with C2 = 62 pF (top-right). Waveforms in the bottom plot are also measured with C2 = 62 pF but under the BCF-12 scintillation light, representing the realistic pulses one can see with the NDL EQR20 SiPM from a scintillator-based hadron calorimeter.

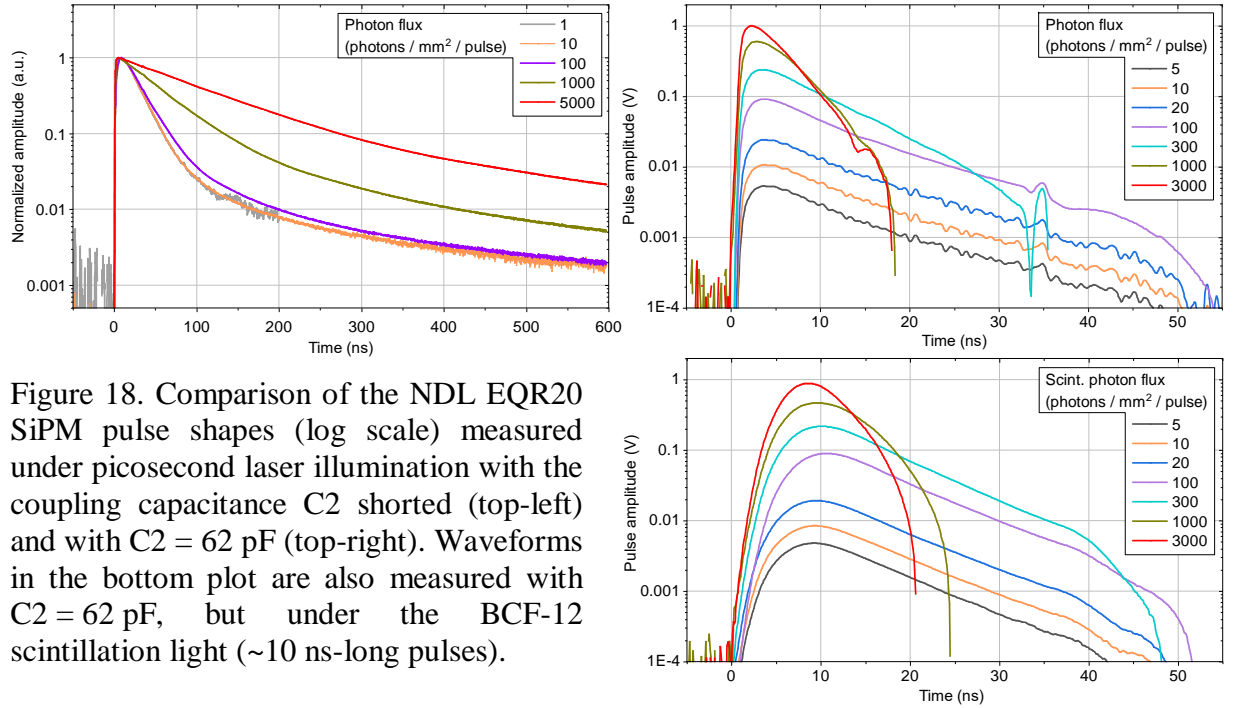


Figure 18. Comparison of the NDL EQR20 SiPM pulse shapes (log scale) measured under picosecond laser illumination with the coupling capacitance C2 shorted (top-left) and with C2 = 62 pF (top-right). Waveforms in the bottom plot are also measured with C2 = 62 pF, but under the BCF-12 scintillation light (~10 ns-long pulses).

As could be seen from Fig.14 (left) and Fig. 15 (left), rising edge of the NDL pulse varies from ~3 ns down to ~1 ns as the result of the distortion. It therefore can heavily affect the results of time-of-arrival (TOA) measurement for the case of detecting light flashes shorter than that. However, the decay time of most scintillators is larger, including the BCF-12 scintillation fibers used to measure the pulse shapes presented in Fig.18 (bottom). In that case, the NDL pulse shape distortion affects TOT readings only, without introducing a significant TOA error.

The possible advantage of the EQR20 SiPMs in terms of the effect of radiation damage discussed in Sec.1 becomes unjustified at higher dark count rates since many pixels will be “fired” at any given time, therefore increasing the microcell occupancy and widening the pulse shape for both signal and noise pulses.

5. Conclusions

NDL EQR20 SiPMs feature a set of remarkable performance characteristics independently determined by our study. A PDE as high as 50% combined with the large sensitive area (39 mm²), gain of up to 10⁶, and pulses as narrow as 1.5 mV/pC can make them the photosensors of choice in specific applications like, e.g., ring imaging Cherenkov detectors. Mediocre levels of correlated noise and non-ideal stability of the pulse shape at various overvoltages are among the non-critical disadvantages of the EQR technology.

However, the strong pulse shape distortion starting at 1% occupancy will overly complicate the use of the NDL EQR20 SiPMs in detection of signals of a wide dynamic range, such as e.g. scintillator-based hadron calorimetry.

Acknowledgement

I. Bearden, S. Jia, I. P. Møller and the ALICE FoCal-H project, through which all the studied SiPMs were acquired, gratefully acknowledge support from The Carlsberg Foundation (CF21-0606) and the Danish Council for Independent Research/Natural Sciences.

Sofia University acknowledges support by the European Union - NextGenerationEU through the National Recovery and Resilience Plan of the Republic of Bulgaria, project SUMMIT BG-RRP-2.004-0008-C01. V. Buchakchiev acknowledges support from ESA through contract number 4000142764/23/NL/MH/rp.

References

- [1] P. Buzhan et al., Silicon photomultiplier and its possible applications, NIM A 504 (2003) 48–52, [https://doi.org/10.1016/S0168-9002\(03\)00749-6](https://doi.org/10.1016/S0168-9002(03)00749-6).
- [2] A. Ghasemi, K. Sato and K. Kobayashi, [A technical guide to silicon photomultipliers \(MPPC\)](#), Hamamatsu Photonics K.K., KAPD9005E01 Mar. 2017.
- [3] Hongmin Liu et al., High-density silicon photomultipliers with epitaxial quenching resistors at Novel Device Laboratory, JPS Conf. Proc., 011002 (2019) <https://doi.org/10.7566/JPSCP.27.011002>.
- [4] Hamamatsu Photonics K.K., [S13360 series MPPCs for precision measurement datasheet](#), KAPD1052E05 Oct. 2022 DN.
- [5] Jiali Jiang et al., Recovery time of silicon photomultiplier with epitaxial quenching resistors, Instruments 2017, 1, 5, [doi:10.3390/instruments1010005](https://doi.org/10.3390/instruments1010005).
- [6] NDL EQR20 Series SiPM datasheet, <http://www.ndl-sipm.net/PDF/Datasheet-EQR20.pdf>.
- [7] ALICE collaboration, Technical Design Report of the ALICE Forward Calorimeter (FoCal), CERN-LHCC-2024-004, ALICE-TDR-022, July 17, 2024 <https://cds.cern.ch/record/2890281>.
- [8] I. Béjar Alonso et al., High-Luminosity Large Hadron Collider (HL-LHC): Technical design report, CERN Yellow Reports: Monographs, CERN-2020-010 (CERN, Geneva, 2020), [doi:10.23731/CYRM-2020-0010](https://doi.org/10.23731/CYRM-2020-0010).
- [9] Y.A. Melikyan et al., Characteristic properties of Planacon MCP-PMTs, 2021 JINST 16 P12032, <https://doi.org/10.1088/1748-0221/16/12/P12032>.
- [10] PicoQuant GmbH, [PDL 800-B Picosecond pulsed diode laser driver datasheet](#), January 2018.
- [11] V. Chmill et al., On the characterisation of SiPMs from pulse-height spectra, NIM A 854 (2017) 70-81, [http://dx.doi.org/10.1016/j.nima.2017.02.049](https://dx.doi.org/10.1016/j.nima.2017.02.049).
- [12] Semiconductor Components Industries, LLC, [OnSemi J-Series SiPM sensors datasheet](#), MICROJ-SERIES/D, August, 2021 – Rev. 7
- [13] Robert Klanner, Characterisation of SiPMs, NIM A 926 (2019) 36–56 <https://doi.org/10.1016/j.nima.2018.11.083>
- [14] Zhiyu Zhao et al., Dynamic range of SiPMs with high pixel densities, [arXiv:2407.17794v1](https://arxiv.org/abs/2407.17794v1).